GEOLOGY

Past intrusion of Circumpolar Deep Water in the Ross Sea: Impacts on the ancient Ross Ice Shelf

Chiara Pambianco[1,2]*, Alessio Nogarotto[2], Mathia Sabino[3], Lucilla Capotondi[4], Francesca Battaglia[2], Federico Giglio[2], Gesine Mollenhauer[5,6], Jens Hefter[5], Alessio Di Roberto[7], Simon T. Belt[8], Enrico Pochini[9], Francesco Muschitiello[10], Andrea Geniram[11], Ester Colizza[11], Giulia Giorgetti[4,12], Fiorenza Torricella[2,11], Tommaso Tesi[2]

The Ross Ice Shelf, Antarctica's largest by area, may face increased instability under future warming, threatening the Antarctic Ice Sheet. Understanding its past response to climate change is critical for anticipating future sea-level rise. We present a multi-proxy reconstruction of ocean and cryosphere conditions in the Ross Sea over the past 40,000 years. Our data show that warm Circumpolar Deep Water reached the JOIDES Trough in the western Ross Sea shortly after the Last Glacial Maximum, coinciding with the retreat of an ancestral ice shelf. This oceanic warming aligns with a southward shift of both the westerly and easterly wind belts, indicating a large-scale atmospheric mechanism driving regional ocean changes. The timing and nature of these processes reveal the tight coupling between atmospheric circulation, ocean heat transport, and ice shelf dynamics. These interactions led to reduced ice shelf extent, highlighting the role of ocean-atmosphere coupling in the Pacific sector of the Southern Ocean during deglaciation.

INTRODUCTION

With almost 60 m of sea level equivalent, the Antarctic Ice Sheet (AIS) can substantially affect the global rise of sea level in a global warming scenario (*1*–*3*). However, predictions of future sea level rise remain challenging due to the high degree of uncertainty about the response of the AIS to climate change, particularly its marine-based sectors that follow mechanisms of rapid ice shelf disintegration and grounding line retreat, collectively referred to as Marine Ice Sheet Instability (MISI) (*4*, *5*). Ice flow acceleration and thinning are currently observed in the West AIS (WAIS), which has the potential to raise sea level by about 5 m (*5*). Thwaites Glacier is also exhibiting the largest changes of any other ice-ocean system in Antarctica (*5*, *6*) along with Amundsen Sea embayment (*7*) and Pine Island Bay (*8*). While West Antarctica contains more than two-thirds of its ice volume grounded above sea level (*9*) the East AIS (EAIS) holds an order-of-magnitude higher sea level equivalent (i.e., more than 50 m), with large sectors of marine-based ice sheets sensitive to oceanic and atmospheric warming (*1*–*3*). The Ross Ice Shelf (RIS) acts as a critical buttress for both the WAIS and the EAIS, stabilizing ice flow and supporting a catchment basin that holds ~11.6 m of potential sea level rise in water-equivalent terms (*10*) and has undergone partial or full collapse during past warm periods (*2*, *11*). Ice mass loss can be promoted by various mechanisms, including the incursion of warm Circumpolar Deep Water (CDW) on the continental shelf, reaching shelf cavities and glacier grounding lines (*4*, *5*, *12*). This can weaken the buttressing effect of ice shelves and destabilize upstream ice flow (*13*), potentially contributing to the MISI (*4*, *14*). Modern mechanisms for CDW advection and basal ice melt appear to be closely dependent on wind migration patterns, particularly the Westerlies, as currently documented in the Bellingshausen Sea and Amundsen Sea (*15*), the Dronning Maud Land (*16*), and the western Antarctic Peninsula (*15*). Similar wind-ocean dynamics have been extensively investigated in the Polar Front during the last deglaciation in studies primarily focusing on wind-driven upwelling and CO_2 release (*17*), CDW signature (*18*), and regional patterns (*19*). These previous studies might, thus, imply that the migration of westerly winds could have also promoted the advection of CDW onto Antarctic continental shelves and cavities (*4*, *16*), leaving, however, large uncertainties regarding the actual oceanic patterns and modes of retreat of ice masses during last deglaciation. This fundamental knowledge gap stems primarily from the absence of paleo evidence near the grounding line region of Antarctic ice shelves, hindering our understanding of ocean-cryosphere interactions and their influence on the retreat of the marine-based sectors of the AIS. In this study, we investigated a sedimentary sequence recovered via piston coring from the JOIDES Trough (Fig. 1 and fig. S1) strategically located seaward of the paleo grounding line of the ancestral RIS during the Last Glacial Maximum (LGM) (*20*). Although the JOIDES basin is situated on the shelf, where remnants of past glacial cycles are still evident (Fig. 1C), the sediments in this basin were deep enough to remain unaffected by disturbances from the overlying ice sheet, thus allowing for the preservation of an expanded and continuous record of the last deglaciation. In modern times, the JOIDES Trough acts as a pathway for cold bottom water export toward the shelf break, and given its retrograde bed slope with landward-deepening troughs (*20*, *21*), it also promotes the intrusion of salty and warm CDW branches (*22*, *23*), bringing heat and nutrients from the deep open ocean to the continental shelf (*24*). In

[1]University Ca' Foscari of Venezia, 30170 Venezia Mestre, Italy. [2]CNR–National Research Council of Italy, ISP–Institute of Polar Sciences, 40129 Bologna, Italy. [3]Université Libre de Bruxelles, Department of Geosciences, Environment and Society, 1050 Bruxelles, Belgium. [4]CNR–National Research Council of Italy, ISMAR–Institute of Marine Sciences, 40129 Bologna, Italy. [5]Alfred Wegener Institute for Polar and Marine Research, 27570 Bremerhaven, Denmark. [6]Department of Geosciences and MARUM Centre for Marine Environmental Sciences, University Bremen, D-28334 Bremen, Denmark. [7]National Institute of Geophysics and Vulcanology, 56125 Pisa, Italy. [8]Biogeochemistry Research Centre, School of Geography, Earth and Environmental Sciences, University of Plymouth, Drake Circus, Plymouth, Devon PL4 8AA, UK. [9]Department of Earth and Atmospheric Sciences, University of Alberta, Edmonton, Alberta T6G 2E3, Canada. [10]Department of Geography, University of Cambridge, Downing Pl, Cambridge CB2 3EN, UK. [11]Department of Mathematics and Informatics and Geosciences, University of Trieste, 34128, Trieste, Italy. [12]Department of Earth Sciences (DST), University of Firenze, 50121 Firenze, Italy.
*Corresponding author. Email: chiara.pambianco@unive.it

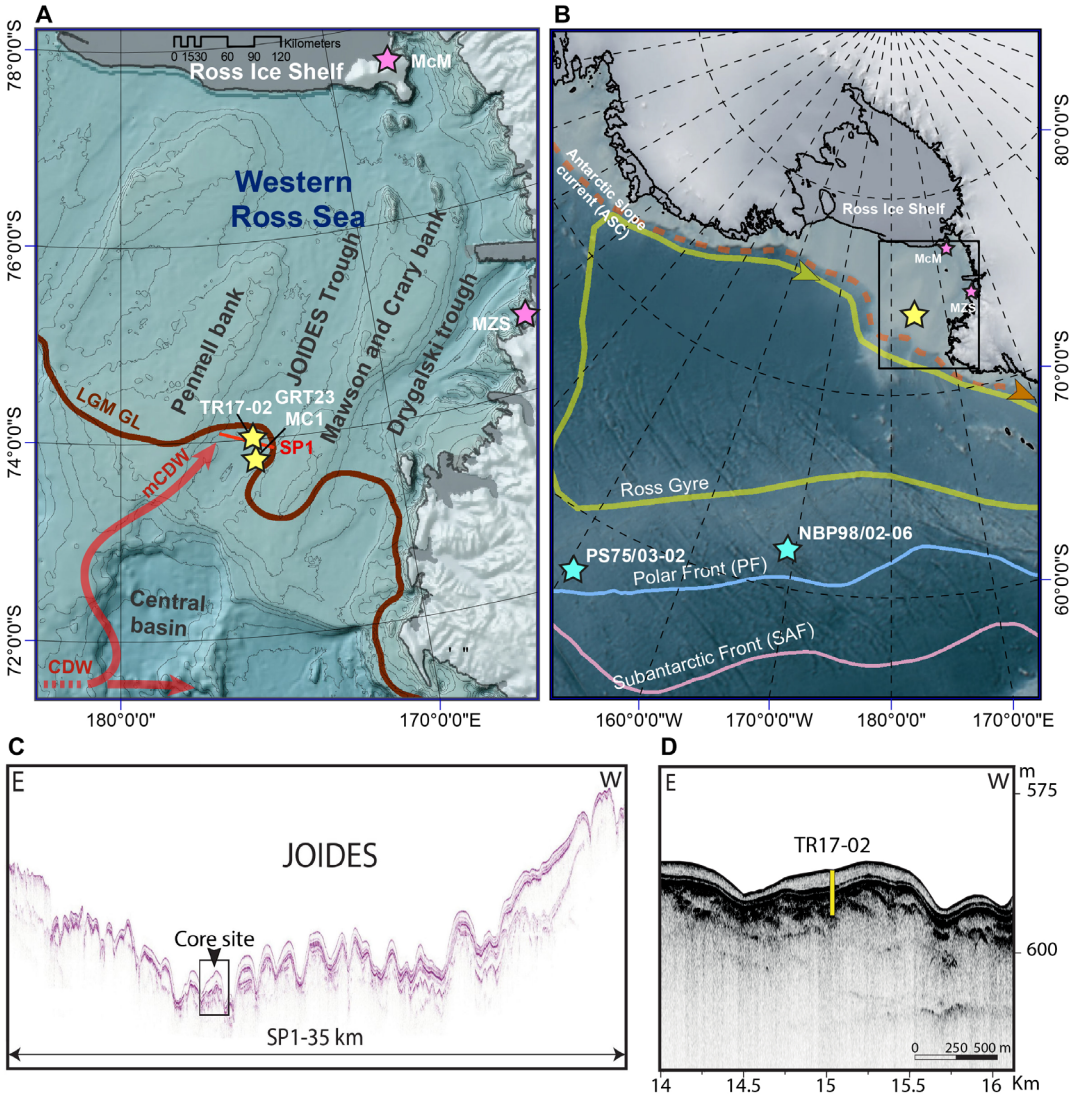

Fig. 1. Map of the study area showing the position of the cores, seismic profile and oceanic features. (**A**) Focus on the JOIDES Trough with respect to the position of cores TR17-02 and GRT23-MC1 over the seismic profile SP1 (red line, fig. S1). The brown line indicates the maximum extent of the ice sheet at the LGM sourced by QAntarctica dataset (*81*). The image highlights the path of CDW from the slope to the shelf, evolving into modified CDW [modified after Morrison *et al.* (*23*) and Bollen *et al.* (*22*)]. Pink stars on the coastal area refer to the Antarctic stations Mario Zucchelli (MZS) and McMurdo (McM). (**B**) Map of the Ross Sea showing the main oceanic features, the Ross Gyre (yellow solid line), the Polar Front (PF; blue solid line), and the subantarctic front (SAF, pink solid line) sourced by QAntarctica on QGis (*81*). Light blue stars indicate two key sediment cores, PS75/03-02 (*18*) and NBP98/02-06 (*17*), which were essential for determining the timing of upwelling dynamics in the polar front. Pink stars refer to the Antarctic stations Mario Zucchelli and McMurdo. (**C**) Transversal seismic profile SP1 depicts the geomorphology of the JOIDES Trough at the coring site, evidencing the large scouring of the submarine topography and the thickness of the sediments (see fig. S1). (**D**) Zoom over the coring site, showing the position of core TR17-02 and sedimentary thickness (see fig. S1).

addition, key evidence comes from geological and stratigraphic records, including the presence of grounding zone wedges (GZWs) and stepwise retreat sequences, which may have favored MISI-driven ice loss (*11*, *20*, *25*).

We used a multiproxy approach to reconstruct past ocean-cryosphere interactions and compared this information with wind-driven dynamics occurring in the open ocean farther north, aiming to disentangle teleconnections occurring between the Polar Front and Ross Sea shelf during the last deglaciation to resolve large-scale mechanisms operating across the Pacific sector of the Southern Ocean. We applied a suite of organic geochemical biomarkers including hydroxylated glycerol dibiphytanyl glycerol tetraethers (OH-GDGTs) produced by Thaumarchaeota to reconstruct past seawater temperature, together with highly branched isoprenoids (HBIs) and phytosterols to resolve the marine ice sheet edge retreat and the onset of ice-free conditions in the JOIDES basin. Along with additional interpretation of foraminiferal assemblages and contextualizing our findings within existing literature, our overarching goal was to provide an unprecedented detail of the initial RIS evolution during the early phase of the last deglaciation and explore how large-scale wind dynamics drove ocean-ice shelf interactions over the shelf of the Ross Sea.

RESULTS

Sediment accumulation rates

We developed an age-depth model for the TR17-02 sediment core using 25 radiocarbon dates calibrated with the Marine20 curve (fig. S4) (*26*, *27*) (six monospecific foraminiferal samples and 19 samples of bulk organic carbon; see Materials and Methods and table S2 for further details). We used the "Rbacon" CRAN package (*28*), applying different local reservoir correction ΔR considering (i) the different matrix and (ii) the ventilation effect during the Marine Isotope Stage 3 (MIS 3), deglaciation and Holocene, following correction for polar regions suggested by Heaton *et al.* (*27*) (see further details on the local reservoir correction in table S1). The strong coherence between the ages of foraminifera tests and bulk organic carbon samples, derived from independent methodologies, supports the validity of the assumptions used to determine ΔR values (table S1). The final age-depth model indicates that sedimentation rates varied across different time periods. During MIS 3 and the LGM [40.5 to 19.0 thousand years (ka) before present (B.P.)], sedimentation rates were relatively low, ~1 cm/ka. The entire deglaciation period, up to the onset of the Holocene, was characterized by relatively high sedimentation rates, ranging from 10 to 35 cm/ka. After ~11.5 ka B.P., sedimentation rates decreased but remained higher than during the glacial period ranging between 14 and 20 cm/ka. These sedimentation rates are consistent with those typically found in this area (*25*, *29*).

Sedimentological framework

Based on the visual core description—color (Munsell Colour Chart), water content (%), grain size proxy (ln Zr/Rb) [sensu (*30*)], and magnetic susceptibility—four distinct sedimentary units were initially identified (Fig. 2). These sedimentological units are named in chronological order, with A being the oldest and D being the youngest, as described below.

Unit A is composed of homogenous and bioturbated dark brown [2.5Y 3/3] silty mud (350.8 to 311.3 cm bsf; 40.5 to 20.4 ka B.P.). The sediment is poorly sorted and is generally fine-skewed. Magnetic susceptibility is very low, around 100 to 150 $\times$ 10^{-5} SI, while water content is around 60%. Benthic foraminifera species occur after 28 ka B.P. where *Globocassidulina subglobosa*, *Miliammina earlandi*, *Stainforthia* sp., and *Trifarina earlandi* are the dominant species. This association is indicative of a distal sub–ice shelf environment (*13*, *31*). Given the description and the coherency with bibliography (*12*), this unit is describing a distal sub–ice shelf environment.

Unit B is composed of poorly sorted dark gray [5Y 4/1] sandy silt (307.8 to 274.3 cm bsf; 19.6 to 16.7 ka B.P.). Downcore, this unit is massive with sparse clasts, while in the upper part it is homogeneous. Magnetic susceptibility is high (around 500 $\times$ 10^{-5} SI), indicating a high input of terrigenous and coarse detrital material from a nearby grounding line (*32*, *33*). The ln(Zr/Rb) values indicate a grain size decrease toward the top of the unit. An exceptional abundance of well-preserved benthic and planktic foraminifera were found in this unit. The foraminifera assemblages comprise benthic species such as *Astrononion echolsi*, *Cibicides* spp., *Globocassidulina biora*, *Globocassidulina subglobosa*, *Cassidulinoides* spp., *Nonionella* spp., *Stainthforthia concava*, *Trifarina earlandi*, and planktic species such as *Neogloboquadrina pachyderma*, all indicative of a sub–ice shelf environment (*12*, *25*). Of particular note is the presence of *T. earlandi* with spines (fig. S5), which is associated with high hydrodynamics and extreme conditions (*34*). *T. earlandi* increases in absolute abundance at 17.9 ka B.P. (301.5 cm bsf), 17.1 ka, and 16.1 ka B.P. (289 and 282 cm bsf). The co-occurrence of spined and costate *T. earlandi* (fig.S5) may suggest intense bottom currents prior and/or during the initial phase of ice shelf breakup, similar to previous observations in the Whales Deep basin (*12*, *35*). We interpret this unit representative of a calving zone.

Unit C is composed of a dark green [10GY 2/4] silty mud matrix (270.8 to 263.8 cm bsf; 16.7 to 16.5 ka B.P.). This unit is a massive and calcareous foraminifera barren section. The magnetic susceptibility profile shows a rapid decrease throughout the unit to 200 and 100 $\times$ 10^{-5} SI, pointing to a progressive reduction of terrigenous material and an increase from a biogenic source. Given these characteristics and the coherency with bibliography (*12*), we interpret this unit is reflecting a distal sub–ice shelf environment.

Unit D consists of massive homogeneous olive [5Y 4/3] silty mud with sparse pebbles in some sections and occasional sandy and gravelly lenses (260.3 to 2.5 cm bsf; 16.4 to 1.45 ka B.P.). The degree of bioturbation varies markedly within the unit. No calcareous foraminifera were observed within this unit. The sediment is poorly sorted but is generally fine-skewed. Punctual transitions to sand and gravel lenses within the sediment core result in a variable magnetic susceptibility profile downcore. The water content in the sediment is around 60%. The magnetic susceptibility shows low values (<1 $\times$ 10^{-5} SI), pointing to a very high content of biogenic material, except for the sandy lenses where the magnetic susceptibility values are around 150 $\times$ 10^{-5} SI, suggesting a higher input of terrigenous material. This unit likely indicates an open marine environment with occasional input of ice-rafted debris (IRDs) from melting icebergs (*12*).

Biomarkers

We used a suite of complementary biomarkers to investigate the cryosphere-ocean-climate interactions and understand how the sedimentary units previously identified reflect different paleo-environmental conditions. We measured hydroxylated glycerol dibiphytanyl glycerol tetraethers (OH-GDGTs; membrane lipids produced by Thaumarchaeota), HBIs, and phytosterols to reconstruct past seawater temperatures and fast-ice distribution and resolve the retreat of the marine ice sheet edge and the onset of ice-free conditions in the Ross Sea.

Proxies based on membrane lipids, particularly the hydroxylated index of OH-GDGTs, have become popular tools for subsurface ocean temperature (SOT) reconstructions in polar regions (*31*) and, in particular, within the Antarctic marginal seas (*36*, *37*). The rapid development of this proxy is well-reflected by numerous calibration curves available in the literature (*38*–*40*). In this study, we use the calibration provided by Lü *et al.* (*40*), which exhibits values for the late Holocene that are the most consistent with modern water mass temperature observations in the sub-surface region of the JOIDES basin (table S3 and fig. S6) (*41*, *42*). However, given the evolving nature of these calibrations, we took into consideration the relative changes in paleo-temperatures rather than their absolute values. Further details about the different calibrations available in the literature can be found in table S4.

Furthermore, we measured the HBI biomarker $IPSO_{25}$ ["Ice Proxy for the Southern Ocean with 25 carbon atoms" (*43*)] to determine fast ice occurrence (ice shelf edge system), along with HBI III and brassicasterol as indicators for open marine productivity (*44*). By combining information from sedimentology and biogeochemistry, we described the detailed paleo-environmental evolution of the area through the different facies, previously identified (see above),

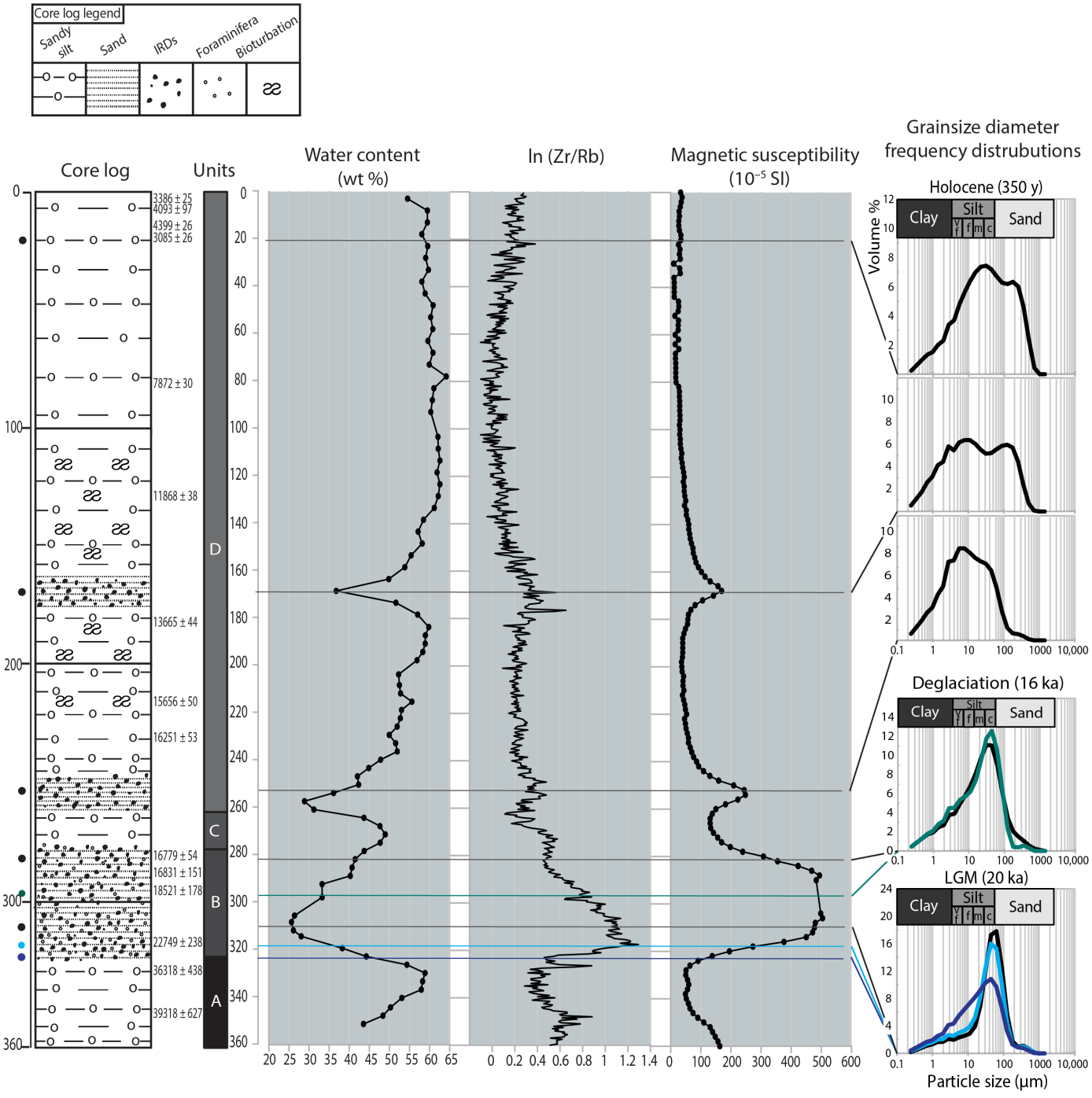

Fig. 2. Representative downcore sedimentary succession for core TR17-02. The left panel shows the core log and subsampling positions for grain size and radiocarbon dating. Aside from the core log, the boxes labeled from (A) to (D) and highlighted in different shades of gray indicate the sediment units identified within the core. The right panels show calculated water content, core matrix grain size proxy ln(Zr/Rb), magnetic susceptibility, and representative grain size frequency distribution for each coarse sample. The assumption is that the elemental ratio of Zr/Rb increases with increasing grain size in the fine fractions (<63 µm) and decreases with increasing grain size in the >63-µm fraction, following the indications of Wu *et al.* (*30*) who tested this proxy in the JOIDES Trough.

as follows: Unit A, distal sub–ice shelf; unit B, calving zone; unit C, ice shelf edge; unit divided into two sub-units, open marine-high productivity (D1); open marine-low productivity, (D2).

In the distal sub–ice shelf unit (unit A, 40.5 to 20.4 ka B.P.), paleo-SOT shows a decreasing trend from 40 ka B.P. to the LGM, indicating a general cooling consistent with the final stages of MIS 3 (Fig. 3J). $IPSO_{25}$ and HBI III show particularly low fluxes (Fig. 3, G and H) or below detection limits (see Materials and Methods), suggesting the presence of permanent ice cover in the area (*43*, *45*). Brassicasterol (Fig. 3I) shows low fluxes (0.005 ± 0.005 μg/cm^2 per year), possibly due to water advection below the ice shelf and tidal excursion.

In the calving zone unit (unit B, 19.6 to 16.7 ka B.P.), the reconstructed SOT exhibit the lowest values observed in the whole record, which is consistent with the climate period during the LGM (Fig. 3J). $IPSO_{25}$, HBI III (0.011 ± 0.021 and 0.006 ± 0.008 ng/cm^2 per year, respectively, Fig. 3, G and H), and brassicasterol (0.028 ± 0.027 μg/cm^2 per year; Fig. 3I) fluxes are low, thus indicating an ice-covered configuration similar to unit A. Overall, despite these two units showing similar characteristics for HBIs and brassicasterol, the benthic foraminiferal association previously discussed, in combination with sedimentological evidence, allows us to differentiate between these two sub–ice shelf environments.

The ice shelf edge unit (unit C, 16.7 to 16.5 ka B.P.) is characterized by the highest $IPSO_{25}$ fluxes of the whole core (0.140 ± 0.052 ng/cm^2 per year; Fig. 3G). Within this unit and before the $IPSO_{25}$ peak, we observed a sharp increase in SOT (Fig. 3J), which reflects the rapid change of oceanic forcing and the overall reorganization of the water column within the study area.

HBI III fluxes exhibits a similar trend, albeit with lower values (0.027 ± 0.006 ng/cm^2 per year). In contrast, fluxes of brassicasterol (Fig. 3I) remain relatively stable (0.031 ± 0.020 μg/cm^2 per year) with a similar trend to that seen in units A and B. The sharp peak of $IPSO_{25}$ at 16.6 ka B.P. suggests the rapid onset of an environment where an ice shelf edge was present, but where also light was present, to allow the blooming of sympagic diatoms growing within the seasonal fast ice that seasonally develops at the edge of an ice shelf. Thus, the abrupt increase of $IPSO_{25}$ documents the retreating ice shelf edge and its position during the early deglaciation in the JOIDES basin. The change in water mass properties is also confirmed by the progressive disappearance and lack of preservation of calcareous foraminifera, possibly linked to a change in alkalinity.

Based on the biomarker data, Unit D (16.4 to 1.45 ka B.P.) has been divided into two sub-units, D1 and D2. Unit D1 (16.4 to 12.3 ka B.P.) is characterized by a bioturbated silty mud matrix, with the highest fluxes of HBI III and brassicasterol in the whole record (0.062 ± 0.035 ng/cm^2 per year and 0.079 ± 0.046 μg/cm^2 per year; Fig. 3, H and I, respectively). Along with lower $IPSO_{25}$ fluxes (0.020 ± 0.012 ng/cm^2 per year; Fig. 3G), this large increase of these pelagic biomarkers suggests that, during the deglaciation, more open water conditions and associated blooming of primary producers prevailed at the coring site, implying a further retreat of the ice shelf edge and a decrease in sea ice cover. Consistent with this interpretation, the SOT shows a general warming with temperatures coherent with modern CDW temperatures (table S3 and fig. S6).

Last, the open marine-low productivity unit D2 (12.0 to 1.45 ka B.P.) consists of homogeneous silty mud showing poor bioturbation and reduced fluxes of HBI III and brassicasterol (0.013 ± 0.006 ng/cm^2 per year and 0.032 ± 0.010 μg/cm^2 per year, respectively). Very low fluxes of $IPSO_{25}$ indicate an even more distant position from the

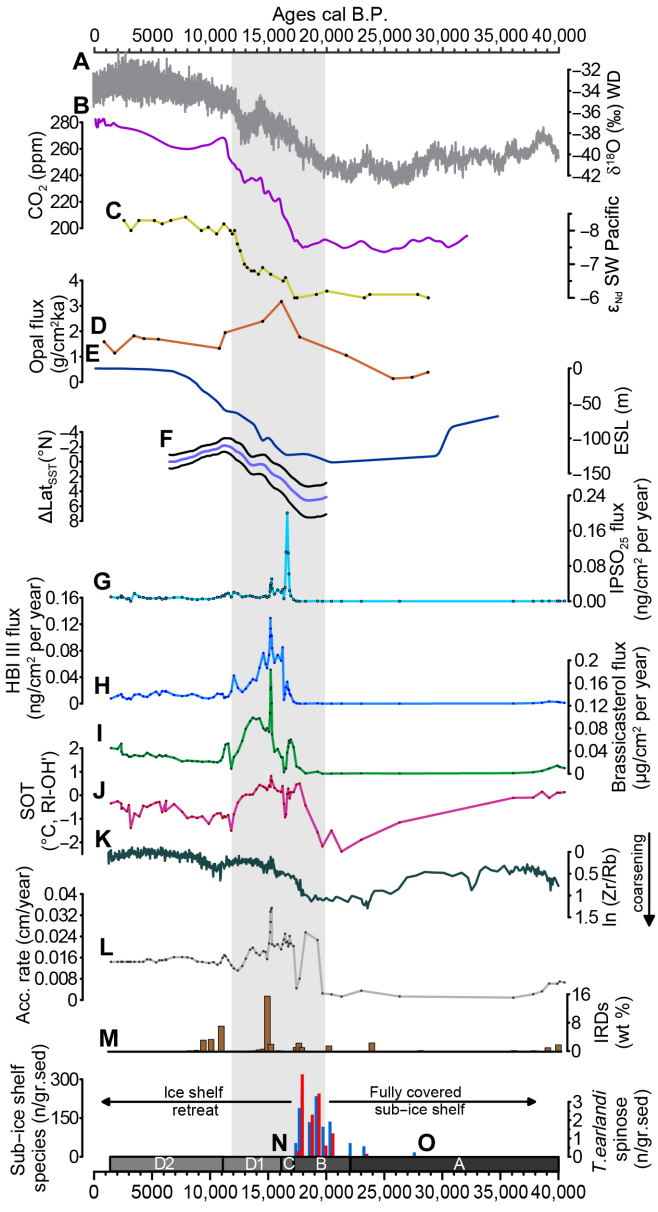

Fig. 3. Poleward migration of the westerly winds over the last deglaciation and their connection with Ross Sea climate reorganization. (**A**) Global temperature warming from Wais Divide ice core from (*64*) (gray) and (**B**) atmospheric CO_2 from (*82*) (purple). In yellow, (**C**) CDW upwelling from core PS75/03-02 from (*18*). (**D**) Opal flux from core NBP98/02-06PC (orange) testifying wind-driven upwelling during the last deglaciation retrieved by Anderson *et al.* (*17*). (**E**) Global sea level rise estimated by Lambeck *et al.* (*83*)(deep blue). (**F**) Poleward shift of westerly winds recorded by Gray *et al.* (*19*) during last deglaciation (purple and gray line). (**G**) Fluxes of $IPSO_{25}$ (light blue), (**H**) HBI III (blue), (**I**) brassicasterol (green), and (**J**) SOT records following the calibration curve of Lü *et al.* (*40*). Sedimentological information including (**K**) matrix grainsize proxy (ln Zr/Rb) along with (**L**) accumulation rates and (**M**) IRD (%) counts are plotted as a bar chart. The bottom chart indicates the presence of foraminifera from both species [(**N**) sub–ice shelf association in blue and (**O**) *T. earlandi* in red]. Accelerator mass spectrometry (AMS) ^{14}C age constraints in calibrated before present (B.P.) are presented at the top bar. The vertical box highlighted in gray marks the deglaciation [19 to 11 ka B.P. as time interval defined by Clark *et al.* (*84*)]. Boxes at the bottom indicated the biogeochemical units previously described [(A) distal sub–ice shelf, (B) calving zone, (C) ice shelf edge, (D1) open marine with enhanced upwelling, and (D2) open marine with decreased upwelling]. ppm, parts per million.

ice shelf edge and fast-ice region. This unit was characterized by a reduced abundance of open water biomarker proxies, suggesting relatively lower productivity than the early deglaciation, together with a decrease of SOT (Fig. 3J) yet much higher than the LGM.

DISCUSSION

Ocean-ice shelf interactions and possible connections with Polar Front dynamics

While many previous reconstructions have focused on the retreat of the AIS in the Ross Sea sector (*11*, *20*, *21*, *25*, *46*) the early evolution and positioning of the paleo RIS since the LGM remains poorly investigated. Low sedimentation rates (Fig. 3l) and productivity (Fig. 3, H and I) during MIS 3 and LGM indicate that the JOIDES basin was permanently covered by an ice shelf (Fig. 4A). During this period, the SOT record indicates a gradual cooling throughout MIS 3, reaching the lowest values at the LGM (Fig. 3J). Furthermore, benthic foraminiferal assemblages at the LGM further confirm the presence of a sub–ice shelf environment (Fig. 3, N and O).

At the onset of the deglaciation, our multiproxy data precisely track the time-transgressive modification of the outer part of the paleo-RIS (Fig. 4B). Specifically, because $IPSO_{25}$ is biosynthesized by certain sympagic diatoms (i.e., *Berkeleya adeliensis*) that thrive within platelet ice (*43*) commonly found beneath fast-ice at the ice shelf edge, the sharp peak observed in our record (Fig. 3G) is a clear indication that the ice shelf edge was located at the core site around 16.6 ka B.P. (Fig. 4C). This finding indicates a substantial transformation in the ice shelf's configuration within the JOIDES region, transitioning from a sub–ice shelf setting to an ice shelf edge environment. Subsequently, HBI III and brassicasterol (Fig. 3, H and I) collectively indicate that the JOIDES further transitioned toward high-productive open water conditions between 16 and 11 ka B.P. (Fig. 4D). The extensive phytoplankton blooms, in fact, could only commence after light ceased being a limiting factor. If now we take the SOT into consideration, then it is evident that the ice shelf modifications just described are well-coupled with the SOT anomalies (~+2°C). In particular, the concurrent increase in sub-surface temperature (Fig. 3J) and primary productivity (Fig. 3, H and I) points toward the presence of a relatively warm, nutrient-rich water mass in the JOIDES Trough, likely reflecting the CDW intrusion over the margin. Thus, given the time-transgressive changes observed at the ice sheet edge, our biomarker findings suggest the intrusion of modified circumpolar deep water (mCDW) over the margin that likely played a pivotal role in initiating the retreat of the ice shelf in the JOIDES basin (Fig. 4, C and D).

The timing of SOT and primary productivity anomalies (~18 to 12 ka B.P.) closely mirror well-known processes documented in the Polar Front, notably (i) the southward shift of the westerly winds (Fig. 3F), (ii) the general re-organization of the water column structure (Fig. 3C), and (iii) high opal fluxes (Fig. 3D). For example, Gray *et al.* (*19*) described a poleward shift of westerly winds during this period (19 to 12 ka B.P.) (Fig. 3F) that may have influenced the Southern Ocean nutrient upwelling (Fig. 3D) (*17*).In the Pacific sector of the Polar Front, neodymium isotope data (PS7503-02; Figs. 1 and 3C) from deep to abyssal waters (*18*) suggest widespread water column destratification and reorganization during the last deglaciation. As a result, the primary production in the Pacific sector of the Polar Front increased substantially in response to wind-driven nutrient upwelling (NBP98/02-06; Figs. 1 and 3D), combined with venting of CO_2 from old and deepwater masses previously isolated from the atmosphere (Fig. 3B) (*17*). In summary, the observed synchronicity between our proxy records and previously documented climate patterns farther north strongly suggests the presence of a common mechanism operating across the Pacific sector of the Southern Ocean echoing over the continental margin during last deglaciation.

Last, during the Holocene, our record documents a second important water column reorganization (Fig. 4E). This period is characterized by oceanic cooling (Fig. 3J) combined with a sharp decline in primary productivity proxies (Fig. 3, H and I), indicating an open but less productive marine environment compared to the deglaciation period, despite a retreating ice shelf system that should release a large amount of macro and micro nutrients (*47*, *48*). Overall, this further supports the role of the CDW advection during last deglaciation that likely played first-order control on the primary productivity in the JOIDES region.

Role of the westerlies and further mechanisms

While the influence of westerly wind migration on upwelling and primary productivity in the Polar Front during the last deglaciation is well-established (*17*, *19*, *24*), its impact on the Ross Sea continental shelf, particularly regarding ocean-ice shelf interactions, remains poorly investigated. Our results reveal a potential connection between changes in large-scale wind patterns and the initial RIS retreat. Today, the JOIDES Trough is one of the major conduits of mCDW intrusion over the Ross Sea shelf (*22*, *23*, *42*). However, in modern conditions, the exchange of warm and nutrient-rich mCDW from the slope to the shelf is highly limited by the Antarctic Slope Front (ASF) that defines the southernmost component of the Ross Gyre (Fig. 1A) (*42*, *49*). In modern conditions, upwelling of mCDW onto the shelf occurs primarily during events of outflows of high-salinity and dense shelf water originating from polynyas (i.e., dense-water shelf setting) (*23*, *50*–*52*). Our results might therefore suggest that the Slope Current and associated ASF were relatively weak during the last deglaciation, allowing more CDW transport over the margin. This process is well-documented in other regions, such as East Antarctica, where the weakening of the Antarctic Slope Current enhances ocean heat intrusions toward the Totten Glacier (*53*). Given the role of the easterlies in driving the strength of the ASF (*54*, *55*) and the agreement between our record and ocean dynamics documented around the Polar Front, it is reasonable to propose a large-scale reorganization driven by the southward migration of westerlies and easterlies.

Spence *et al.* (*55*) assessed the impact of shifts in the westerlies and easterlies on the heat exchange for the Antarctic Peninsula. Their model simulates rapid warming over the margin from an advective heat flux induced by weakened near-shore surface Ekman pumping in response to weakened easterly winds. This in turn decreases the strength of the coastal and slope current promoting the advection of CDW over the margin. In light of this proposed mechanism, the migration of the westerlies and easterlies farther south during the last deglaciation might have resulted in a dynamic interplay between coastal winds, coastal currents, and heat transport across a weakened ASF promoting the retreat of the ancestral RIS. In modern conditions, the Ross Gyre is bounded by the Polar Front of the Antarctic Circumpolar Current to the north, the Antarctic Slope Current to the south. Historical reconstructions of the Ross Gyre variability are scare. Its behavior is strongly driven by wind pattern (*56*), and in the western Ross Sea, Tolotti *et al.* (*57*) suggested a

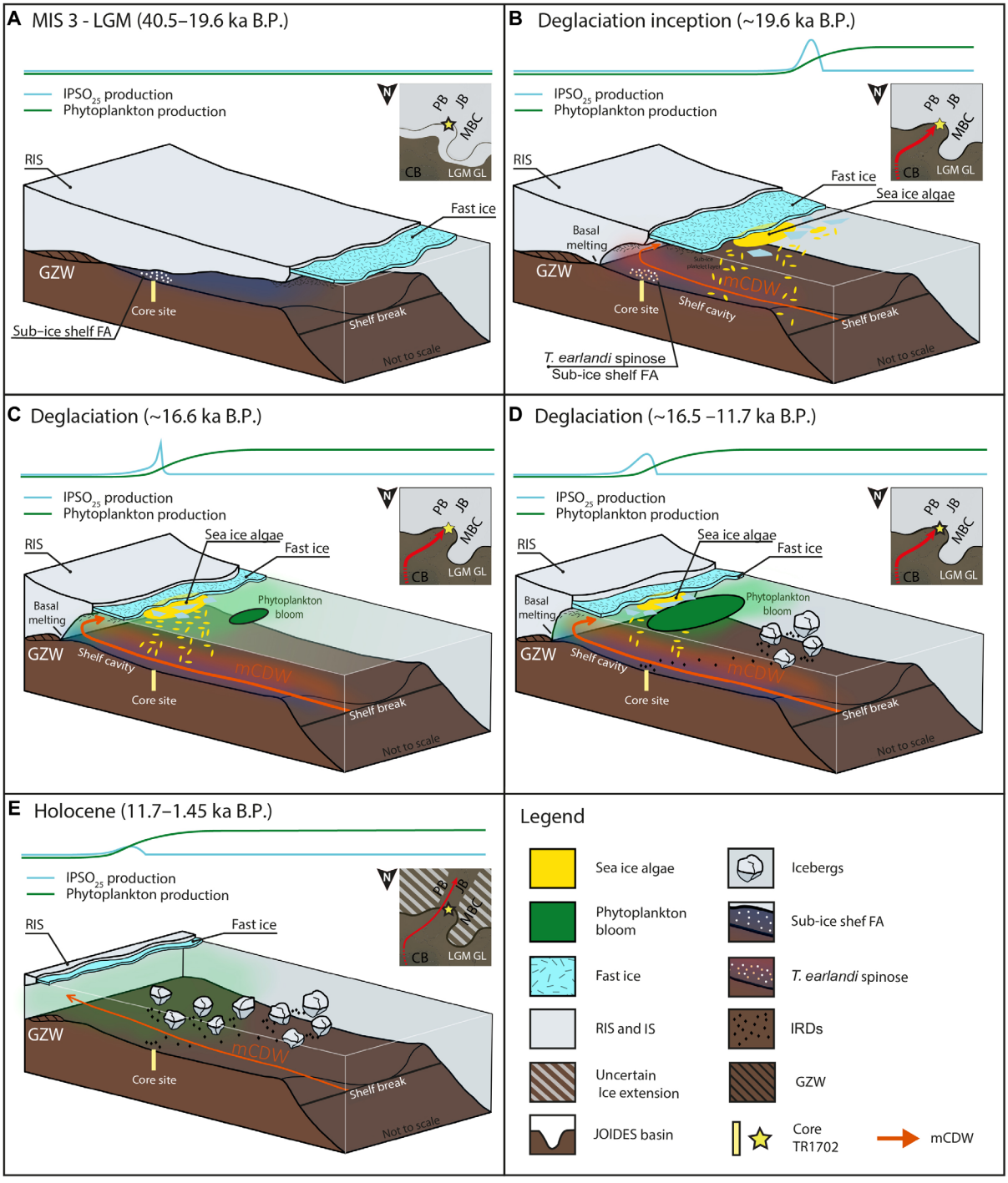

Fig. 4. Cartoon describing the retreat in the Ross Sea (JOIDES Trough) from MIS 3-LGM to Holocene. At the top right of each panel is shown the narrow JOIDES Trough geography and the early formation of the proposed embayment (JB, JOIDES basin; PB, Pennel Bank; MBC, Mawson and Crary Bank; CB, Central Basin), and red arrow indicates mCDW impinging from the outer shelf [modified after Prothro *et al.* (*25*) and Bollen *et al.* (*22*)]. Graphs on the top of each snapshot are showing the trend of $IPSO_{25}$ and phytoplankton production, fingerprint of fast ice, and open marine conditions, respectively. (**A**) Full ice shelf coverage during the MIS 3 and the LGM. White dots indicate the presence of sub–ice shelf foraminifera association. (**B**) Deglaciation inception and intrusion of mCDW driven by poleward shift of westerly winds, enhancing the melting of the floating ice shelf and sea algae production. White and pink dots indicate the co-occurrence of sub–ice shelf foraminifera association and *T. earlandi* spinose, species that is associated with high hydrodynamics and extreme conditions (*34*). (**C**) Situation within the advanced deglaciation (16.6 ka B.P.), mCDW is bringing heat causing the RIS to retreat southward, and this is detected by the highest peak in the $IPSO_{25}$ record. (**D**) Deglaciation (16.5 to 11.7 ka B.P.) marked by heat and nutrient upwelling driven by mCDW, which allows the blooming of pelagic plankton and enhancing the ice shelf retreat and basal melt. At this point, the retreat of the grounded ice occurred within the time frames indicated by the available literature (approximately after 13 ka B.P.). (**E**) Snapshot at the onset of the Holocene, setting the conditions for MISI and landward retreat of the ice sheet.

southward shift of the southern limb of the Ross Gyre during last deglaciation, implying a decrease of the Antarctic Slope Current in line with our observations.

Alternatively, freshening derived by either local meltwater production or externally sourced (i.e., meltwater from the Amundsen Sea) could represent another mechanism responsible for ocean warming and ice shelf retreat. Specifically, glacial meltwater and change in the salinity gradients can affect the heat exchange between open waters and continental margins. Using high-resolution models to resolve mesoscale eddies, Si *et al.* (*58*) showed how modern coastal freshening can lead to increased shoreward heat transport in fresh-shelf settings. This implies positive feedback to the RIS retreat that should likely be considered in our interpretation. Similarly, other paleo studies have inferred positive feedback linked to basal meltwater from ice shelves. For example, Silvano *et al.* (*59*) simulated how freshwater can counteract the salt injection during sea ice formation in the Amundsen Sea (warm-shelf setting), preventing full-depth convection and formation of dense shelf water, which allow warm bottom water to reach the ice shelves unaltered, accelerating their basal melt. Similarly, Golledge *et al.* (*60*) have inferred reduced Southern Ocean overturning circulation during meltwater pulse 1A (~14.8 ka B.P.), thus promoting the advection of subsurface warm waters on Antarctic margins and producing positive feedback that further accelerated the ice shelf retreat. Although the western Ross Sea is currently a dense-water setting (*49*), positive feedback driven by freshwater input, as modeled for fresh and warm shelf, could have accelerated the retreat. However, some studies offer a different view highlighting the lack of general consensus. Other simulations, in fact, suggest that meltwater can isolate the margin preventing the heat exchange (*61*, *62*), while other simulations suggest that the freshwater release can even trigger cooling in the Ross Sea (*63*).

Furthermore, warm and highly productive deglacial waters could instead represent an intensification of the polynya activity and dense water export from the Ross margin that, consequently, promoted the intrusion of CDW (*23*). However, freshwater input from melting ice shelves can prevent full-depth convection and the formation of dense shelf water (*59*). Regardless, the presence of a strong polynya seems not to be supported by the core lithology. Specifically, we do not observe evidence of strong bottom currents, such as sediment coarsening, with sediments becoming instead finer at the onset of the deglaciation (low Zr/Rb ratio: Fig. 3K). Last, atmospheric warming at the onset of the deglaciation (*64*) might have promoted the initial ice shelf retreat possibly stimulating primary productivity by releasing micro-nutrients trapped in ice (*47*, *48*). However, the reconstructed SOTs (Fig. 3J) and primary productivity (Fig. 3, H and I) do not mirror the continental Antarctic warming (Fig. 3A). To conclude, among the three proposed mechanisms, the intrusion of warm and nutrient-rich CDW, driven by a southward shift in westerly and easterly winds coupled with the weakening of the ASC (*17*, *19*, *23*, *24*, *49*, *57*), best aligns with the observed dynamics emerging as the most probable hypothesis. More work is needed to further refine the dominant processes, including a fully coupled ocean-atmosphere-cryosphere modeling effort.

Initial embayment in the JOIDES floating ice shelf

Placing our outcomes within the context of a retreating AIS, it is evident that our reconstructed changes occurred much earlier (Fig. 3) than the grounding-line retreat documented in the Ross Sea by other studies (*11*, *20*, *21*, *25*). For instance, using a wide range of atmospheric and oceanic forcings, Lowry *et al.* (*65*) modeled different grounding line retreat rates, with the earliest scenario observed around 14.5 ka B.P., while the rest of the simulations agree on the end of the deglaciation-early Holocene. Similarly, Anderson *et al.* (*11*) and Halberstadt *et al.* (*21*) documented, through sediment cores and geophysical data, a rapid retreat only after 13 cal ka B.P. Recently, Danielson and Bart (*20*) reported the ice sheet grounding duration in the JOIDES middle shelf, with the nearest retreat dated at 13 cal ka B.P. Last, Spector *et al.* (*46*) indicated a rapid grounded ice retreat only occurring since the early Holocene.

Overall, this suggests that the environmental changes documented in the JOIDES Trough reflect the initial reshape of the paleo RIS front driven by ocean-atmosphere-cryosphere interactions preceding the potential MISI (Fig. 4). Specifically, this pattern of retreat implies a fast reduction of the floating ice shelf along the axis of the JOIDES Trough, while the ice sheet was well-pinned above the surrounding banks, generating an embayment along the trough consistent with recent models used to describe the retreat of the grounding line in the Ross Sea (Fig. 4) (*21*, *66*). The rapid formation of an embayment might have directly influenced the ice flow, contributing to the MISI. Specifically, the thinning of an ice shelf and atmospheric warming can increase hydrofracturing leading to more frequent calving events and subsequent ice shelf retreat, which is highlighted by IRDs discharge (Fig. 3M) (*12*). Ice shelves, in fact, play a crucial role in regulating ice discharge from upstream glaciers by attaching to lateral and bottom pinning points, providing buttressing and stabilizing the upstream ice flow (*13*). Instead, the loss of buttressing accelerates ice discharge, while increased basal melting near the grounding line leads to its retreat and further thinning of ice shelves, potentially leading to MISI in the late deglaciation and early Holocene (*4*, *14*).

To conclude, the extent to which the poleward shift of warm CDW intrusions over the Antarctic margins are a recent development or have always been present is a subject of ongoing discussion (*67*). Our record from the Ross Sea precisely reconstructed the time-transgressive formation of the embayment along the JOIDES basin and demonstrated the existence of mCDW at the base of the shelf edge at the beginning of the last deglaciation. The protracted presence of mCDW over the margin coincides with a large-scale atmospheric and oceanic reorganisation documented in the Polar Front. This points toward a common mechanism associated with the southward migration of westerlies and easterlies that, ultimately, regulated the shoreward heat transport onto the Ross margin and possibly favored the retreat of the grounding line during the late deglaciation and early Holocene by reducing the extent of the floating ice shelf. While the precise mechanisms and feedback remain to be elucidated, including the large-scale response in other troughs of the Ross Sea, this study documents large-scale dynamics across the Pacific sector of the Southern Ocean, highlighting the sensitivity of Antarctic ice shelves to oceanic-atmospheric forcing during the last deglaciation. Given the anticipated poleward shift and wind-driven increase in warm mCDW transfer based on 21st century climate projections (*68*–*70*), our findings collectively suggest a substantial reduction of Antarctica ice shelves in the future, as described in our study.

MATERIALS AND METHODS

Sediment core and multicorer

Piston core TR17-02 (74° 01.9995′S, 175° 04.0752′E) was retrieved in the JOIDES Trough on-board of the R/V Italica during the 2017

austral summer in the frame of TRACERS (TephRochronology and mArker events for the CorrElation of natural archives in the Ross Sea) Programma Nazionale di Ricerche in Antartide project. In addition, we used a multicorer (GRT23-MC1) collected in 2023 in the JOIDES Trough to refine the local radiocarbon reservoir correction and estimate the coretop preservation by assessing the "manganese spike" as described by Mangini *et al.* (figs. S2 and S3) (*71*). TR17-02 core is 7.97-m long and was split into 1-m-long sections and stored at 4°C on the vessel. Detailed description of the full core and geophysics acquisition and elaboration (*72*) is available in fig. S1. In this study, we focused on the upper 3.60 m. In the laboratory, split core sections were analyzed using an AVAATECH core scanner for high-resolution image acquisition and XRF analyses (0.5-cm sampling interval). Magnetic susceptibility data were measured every 2 cm along the entire core using a Bartington MS2C loop sensor. Subsequently, sediments were subsampled throughout the core every 5 cm (1-cm-thick intervals) until 178-cm depth and then every 3.5 to 350.8 cm ($n = 82$ samples). All subsamples were stored in 20-ml precombusted glass vials, freeze-dried, and ground for homogenization before analysis at the Institute of Polar Sciences of the National Research Council in Bologna, Italy. The water content (%) and grain size distribution were estimated by weighing samples before and after the freeze-drying procedure (grain size analysis and IRDs counting are thoroughly explained in the Supplementary Materials).

Foraminifera, radiocarbon dating, and age-depth model

Radiocarbon dates include carbonate material from monospecific benthic (*T. earlandi*) and planktonic foraminifera (*N. pachyderma*) ($n = 6$) and bulk organic carbon ($n = 19$) for a total of 25 ($n = 25$) radiocarbon analyses (table S2). Samples selected to isolate foraminifera were treated by gentle washing with distilled water with a 63-μm sieve mesh, and then oven-dried at 40°C on paper filters. The foraminiferal counts was carried out under a binocular stereo-microscope over the >63-μm sediment fraction. Specimen classification followed the taxonomy of Loeblich and Tappan (*73*) and the Antarctic benthic foraminiferal systematic (*74*). All the radiocarbon dates were performed via accelerator mass spectrometry at Alfred Wegener Institute–Mini Carbon Dating System (AWI-MICADAS) laboratory (Bremerhaven). Calibrations of radiocarbon ages obtained from carbon pools are not in equilibrium with the atmosphere and require a correction due to the influence of the reservoir effect (*75*). In addition to the global mean marine reservoir (R) modeled using the Marine20 curve, a further offset (ΔR) needs to be applied to accommodate the local reservoir. The Ross Sea represents a particularly challenging environment for identifying the correct ΔR to use with different datable matrices (table S1). Furthermore, additional care is necessary when targeting the deglaciation time and LGM when the ocean circulation was different from modern conditions. For specific details about the different ΔR values used, see the Supplementary Materials. Our final age-depth model TR17-02 (fig. S4) based on the 25 dates (table S2) was obtained using the "Rbacon" CRAN package (*28*). The congruence between the ages of foraminifera tests and bulk organic carbon samples, determined using distinct methodologies and in particular ΔR values, strengthens the confidence in the assumptions used in calculating ΔR values (table S1).

Bulk data and biomarkers

A total of 80 samples were selected for bulk and biomarker analyses. Around 10 g of freeze-dried samples was powdered and homogenized in an agate mortar. Before the grinding, the coarse fraction comprising coarse sand and gravel (>0.5 mm) was removed from the sediment by manual sieving. Samples were then analyzed for specific biomarkers. Apolar (HBIs) and polar compounds (sterols and GDGTs) were extracted following a modified method from Tesi *et al.* (*76*). A known amount of internal standards [7-hexylnonadecane (7-HND); 9-octylheptadec-8-ene (9-OHD) and 5α-Andro-stan-3β-ol (C46 GDGT)] was added to ~1.0 g of sediments. Samples were left in a 5 wt % KOH and MeOH:H_2O (9:1, v/v) solution at 70°C for 60 min to complete saponification (*76*). The neutral fraction was then extracted from the aqueous solution three times, after centrifugation with pure hexane (HEX). Extracts were dried under N_2 stream and redissolved in a mixture of hexane and dichloromethane (HEX:DCM; 3:2, v/v). Purification was performed using silica gel (60 to 200 μm) columns, preconditioned with pure dichloromethane and HEX. The apolar fraction (containing HBIs) was eluted with HEX and the polar fraction (containing sterols and GDGTs) with MeOH:DCM (1:1, v/v). The apolar dry extract was redissolved in hexane (500 μl) and transferred to (1 ml) GC vials, dried under an N_2 stream, and redissolved in 30 μl of HEX before gas chromatography–mass spectrometry (GC-MS) analysis. The polar fraction was split into two aliquots following the same drying procedure, and then one fraction was redissolved in DCM (500 μl) and transferred to GC vials, dried under an N_2 stream, and redissolved in 500 μl of DCM. This fraction, before GC-MS analysis, was subsampled and derivatized with *N*,*O*-bis(trimethylsilyl)trifluoroacetamide organosilicon compound (BTSFA) and then placed onto a heating plate (15″, 50°C). The other fraction was dissolved in HEX:isopropanol (99:1, v/v) and filtered through a 0.45-μm-sieve PTFE syringe filter. This step was repeated three times to ensure complete retrieval of the compounds from the vial (see "Paleo sub-surface water temperatures" for detailed analytical procedure).

HBIs were quantified via GC-MS using an Agilent 7820a chromatograph fitted with a J&W DB5-MS column (30-m length, 0.25-mm inner diameter, and 0.25-mm film thickness) coupled to a 5977b Mass Selective Detector (MSD) (*76*). The oven temperature ramp was programmed from 60° to 280°C at 10°C/min. During the ramp, the MSD operated in selective ion monitoring (SIM) and SCAN modes. The injection of C8-C40 alkanes (Sigma-Aldrich) was used to further check the retention times of $IPSO_{25}$ and HBI III (*76*). The quantification of $IPSO_{25}$ and HBI III was achieved by integrating peaks of ions mass/charge ratio (*m*/*z*) 348.3 and 346.3, respectively, in SIM mode followed by normalizing to the corresponding peak area of the internal standards (9-OHD;7-HND) and an instrumental response factor obtained by analysis of a purified in-house standard. The identification of retention times of brassicasterol was based on its fragmentation pattern. Brassicasterol was quantified by integrating peaks of 470 *m*/*z* in SIM mode and normalizing the corresponding peak area to that of the internal standard (5α-Andro-stan-3β-ol). Instrumental response factor was calculated using the response of 5α-Andro-stan-3β-ol by comparing the peak areas of these compounds in SIM mode and SCAN mode. Integrated peaks with extremely small areas, and thus, low fluxes (<0.0001 ng/cm^2 per year) were expressed as "nondetectable". Each proxy was then expressed in mass accumulation rate (MAR) calculated by following the methodology proposed by Belt *et al.* (*77*).

Paleo sub-surface water temperatures

Reconstruction of paleotemperatures of seawater masses was performed extracting GDGTs, a class of membrane lipids produced by

certain archaea. Following the procedures previously described by Tung *et al.* (*78*), GDGTs were analyzed on an Agilent 1260 Infinity II ultrahigh-performance liquid chromatography–mass spectrometry (UHPLC-MS) system, consisting of a G1712B binary pump, a G7129A vial sampler with integrated sample thermostat, a G7116A multicolumn thermostat, and a G6125C single quadrupole mass spectrometer with an atmospheric pressure chemical ionization (APCI) ion source. Chromatographic separation of the GDGTs was achieved by coupling two UPLC silica columns (Waters Acquity BEH HILIC, 2.1 mm by 150 mm, 1.7 μm) with a precolumn of 2.1 mm by 5 mm, but with the following chromatographic modifications: mobile phases A and B consisted of n-hexane:chloroform (99:1, v/v) and n-hexane: 2-propanol:chloroform (89:10:1, v/v/v), respectively. The flow rate was set to 0.4 ml/min and the columns were heated to 50°C, resulting in a maximum backpressure of 425 bar. Sample aliquots of 20 μl were injected with isocratic elution for 20 min using 86% A and 14% B, followed by a gradient to 30% A and 70% B within the next 20 min. After this, the mobile phase was set to 100% B, and the column was rinsed for 13 min, followed by a 7-min re-equilibration time with 86% A and 14% B before the next sample analysis. The total run time was 60 min. GDGTs were detected using positive ion APCI-MS and selective ion monitoring (SIM) of (M + H) + ions with the following settings: nebulizer pressure of 50 psi, vaporizer and drying gas temperature of 350°C, and drying gas flow of 5 liter/min. The capillary voltage was 4 kV, and the corona current was +5 μA. The detector was set for the following SIM ions: *m*/*z* 744 (C 46 standard), *m*/*z* 302.3 (GDGT-0), *m*/*z* 1300.3 (GDGT-1), and *m*/*z* 1298.3 (GDGT-2). The resulting scan/dwell time was 66 ms and quantified in relation to the internal standard C46 (*m*/*z* 744). The hydroxylated GDGTs OH-GDGT0 (*m*/*z* 1318), OH-GDGT-1 (*m*/*z* 1316), and OH-GDGT2 (*m*/*z* 1314) were quantified in the scans of their related GDGTs (*79*).

Among different paleothermometers derivable from GDGTs, RI-OH′ is a promising tool for polar regions in rapid development (eq. S1) (*39*, *40*, *80*). However, because of the continuous upgrading of calibration curves for polar areas and the necessity to create local calibration parameters for the Ross Sea, we consider our results as diagnostic evidence for the general water column reorganization, without focusing on the absolute temperature record. We tested different calibration curves (table S4 and fig. S6) and used the curve from (*40*) that better matched the modern values according to our late Holocene record (fig. S6).

Supplementary Materials

This PDF file includes:

Supplementary Text
Figs. S1 to S6
Tables S1 to S4

REFERENCES AND NOTES

1. N. R. Golledge, R. H. Levy, R. M. McKay, T. R. Naish, East Antarctic ice sheet most vulnerable to Weddell Sea warming. *Geophys. Res. Lett.* **44**, 2343–2351 (2017).
2. C. R. Stokes, N. J. Abram, M. J. Bentley, T. L. Edwards, M. H. England, A. Foppert, S. S. R. Jamieson, R. S. Jones, M. A. King, J. T. M. Lenaerts, B. Medley, B. W. J. Miles, G. J. G. Paxman, C. Ritz, T. van de Flierdt, P. L. Whitehouse, Response of the East Antarctic Ice Sheet to past and future climate change. *Nature* **608**, 275–286 (2022).
3. D. J. Wilson, R. A. Bertram, E. F. Needham, T. van de Flierdt, K. J. Welsh, R. M. McKay, A. Mazumder, C. R. Riesselman, F. J. Jimenez-Espejo, C. Escutia, Ice loss from the East Antarctic Ice Sheet during late Pleistocene interglacials. *Nature* **561**, 383–386 (2018).
4. R. M. DeConto, D. Pollard, Contribution of Antarctica to past and future sea-level rise. *Nature* **531**, 591–597 (2016).
5. F. Pattyn, M. Morlighem, The uncertain future of the Antarctic Ice Sheet. *Science* **367**, 1331–1335 (2020).
6. F. S. Paolo, L. Padman, H. A. Fricker, S. Adusumilli, S. Howard, M. R. Siegfried, Response of Pacific-sector Antarctic ice shelves to the El Niño/Southern Oscillation. *Nat. Geosci.* **11**, 121–126 (2018).
7. C. Ritz, T. L. Edwards, G. Durand, A. J. Payne, V. Peyaud, R. C. A. Hindmarsh, Potential sea-level rise from Antarctic ice-sheet instability constrained by observations. *Nature* **528**, 115–118 (2015).
8. D. P. Walker, M. A. Brandon, A. Jenkins, J. T. Allen, J. A. Dowdeswell, J. Evans, Oceanic heat transport onto the Amundsen Sea shelf through a submarine glacial trough. *Geophys. Res. Lett.* **34**, L02602 (2007).
9. J. L. Bamber, R. E. M. Riva, B. L. A. Vermeersen, A. M. LeBrocq, Reassessment of the potential sea-level rise from a collapse of the West Antarctic Ice Sheet. *Science* **324**, 901–903 (2009).
10. K. J. Tinto, L. Padman, C. S. Siddoway, S. R. Springer, H. A. Fricker, I. Das, F. Caratori Tontini, D. F. Porter, N. P. Frearson, S. L. Howard, M. R. Siegfried, C. Mosbeux, M. K. Becker, C. Bertinato, A. Boghosian, N. Brady, B. L. Burton, W. Chu, S. I. Cordero, T. Dhakal, L. Dong, C. D. Gustafson, S. Keeshin, C. Locke, A. Lockett, G. O'Brien, J. J. Spergel, S. E. Starke, M. Tankersley, M. G. Wearing, R. E. Bell, Ross Ice Shelf response to climate driven by the tectonic imprint on seafloor bathymetry. *Nat. Geosci.* **12**, 441–449 (2019).
11. J. B. Anderson, H. Conway, P. J. Bart, A. E. Witus, S. L. Greenwood, R. M. McKay, B. L. Hall, R. P. Ackert, K. Licht, M. Jakobsson, J. O. Stone, Ross Sea paleo-ice sheet drainage and deglacial history during and since the LGM. *Quat. Sci. Rev.* **100**, 31–54 (2014).
12. J. A. Smith, A. G. C. Graham, A. L. Post, C.-D. Hillenbrand, P. J. Bart, R. D. Powell, The marine geological imprint of Antarctic ice shelves. *Nat. Commun.* **10**, 5635 (2019).
13. G. H. Gudmundsson, F. S. Paolo, S. Adusumilli, H. A. Fricker, Instantaneous Antarctic ice sheet mass loss driven by thinning ice shelves. *Geophys. Res. Lett.* **46**, 13903–13909 (2019).
14. R. Reese, G. H. Gudmundsson, A. Levermann, R. Winkelmann, The far reach of ice-shelf thinning in Antarctica. *Nat. Clim. Change* **8**, 53–57 (2018).
15. M. S. Dinniman, J. M. Klinck, W. O. Smith, A model study of Circumpolar Deep Water on the West Antarctic Peninsula and Ross Sea continental shelves. *Deep-Sea Res. Part II* **58**, 1508–1523 (2011).
16. J. Lauber, T. Hattermann, L. de Steur, E. Darelius, M. Auger, O. A. Nøst, G. Moholdt, Warming beneath an East Antarctic ice shelf due to increased subpolar westerlies and reduced sea ice. *Nat. Geosci.* **16**, 877–885 (2023).
17. R. F. Anderson, S. Ali, L. I. Bradtmiller, S. H. H. Nielsen, M. Q. Fleisher, B. E. Anderson, L. H. Burckle, Wind-driven upwelling in the Southern Ocean and the deglacial rise in atmospheric CO_2. *Science* **323**, 1443–1448 (2009).
18. C. Basak, H. Fröllje, F. Lamy, R. Gersonde, V. Benz, R. F. Anderson, M. Molina-Kescher, K. Pahnke, Breakup of last glacial deep stratification in the South Pacific. *Science* **359**, 900–904 (2018).
19. W. R. Gray, C. de Lavergne, R. C. J. Wills, L. Menviel, P. Spence, M. Holzer, M. Kageyama, E. Michel, Poleward shift in the Southern Hemisphere westerly winds synchronous with the deglacial rise in CO_2. *Paleoceanogr. Paleoclimatol.* **38**, e2023PA004666 (2023).
20. M. A. Danielson, P. J. Bart, The staggered retreat of grounded ice in the Ross Sea, Antarctica, since the Last Glacial Maximum (LGM). *The Cryosphere* **18**, 1125–1138 (2024).
21. A. R. W. Halberstadt, L. M. Simkins, S. L. Greenwood, J. B. Anderson, Past ice-sheet behaviour: retreat scenarios and changing controls in the Ross Sea, Antarctica. *The Cryosphere* **10**, 1003–1020 (2016).
22. M. Bollen, C. R. Riesselman, C. Ohneiser, O. Albot, R. McKay, M. K. Lee, K.-C. Yoo, S. Kim, J. I. Lee, R. Levy, Pleistocene oceanographic variability in the Ross Sea: A multiproxy approach to age model development and paleoenvironmental analyses. *Glob. Planet. Change* **216**, 103901 (2022).
23. A. K. Morrison, A. M. Hogg, M. H. England, P. Spence, Warm Circumpolar Deep Water transport toward Antarctica driven by local dense water export in canyons. *Sci. Adv.* **6**, eaav2516 (2020).
24. J. Marshall, K. Speer, Closure of the meridional overturning circulation through Southern Ocean upwelling. *Nat. Geosci.* **5**, 171–180 (2012).
25. L. O. Prothro, W. Majewski, Y. Yokoyama, L. M. Simkins, J. B. Anderson, M. Yamane, Y. Miyairi, N. Ohkouchi, Timing and pathways of East Antarctic Ice Sheet retreat. *Quat. Sci. Rev.* **230**, 106166 (2020).
26. T. J. Heaton, P. Köhler, M. Butzin, E. Bard, R. W. Reimer, W. E. N. Austin, C. Bronk Ramsey, P. M. Grootes, K. A. Hughen, B. Kromer, P. J. Reimer, J. Adkins, A. Burke, M. S. Cook, J. Olsen, L. C. Skinner, Marine20—The marine radiocarbon age calibration curve (0-55,000 cal BP). *Radiocarbon* **62**, 779–820 (2020).
27. T. J. Heaton, M. Butzin, E. Bard, C. Bronk Ramsey, K. A. Hughen, P. Köhler, P. J. Reimer, Marine radiocarbon calibration in polar regions: A simple approximate approach using marine20. *Radiocarbon* **65**, 848–875 (2023).
28. M. Blaauw, J. A. Christen, Flexible paleoclimate age-depth models using an autoregressive gamma process. *Bayesian Anal.* **6**, 457–474 (2011).
29. K. Mezgec, B. Stenni, X. Crosta, V. Masson-Delmotte, C. Baroni, M. Braida, V. Ciardini, E. Colizza, R. Melis, M. C. Salvatore, M. Severi, C. Scarchilli, R. Traversi, R. Udisti, M. Frezzotti, Holocene sea ice variability driven by wind and polynya efficiency in the Ross Sea. *Nat. Commun.* **8**, 1334 (2017).

30. L. Wu, D. J. Wilson, R. Wang, X. Yin, Z. Chen, W. Xiao, M. Huang, Evaluating Zr/Rb Ratio From XRF scanning as an indicator of grain-size variations of glaciomarine sediments in the Southern Ocean. *Geochem. Geophys. Geosyst.* **21**, e2020GC009350 (2020).
31. E. Park, J. Hefter, G. Fischer, M. Hvitfeldt Iversen, S. Ramondenc, E. M. Nöthig, G. Mollenhauer, Seasonality of archaeal lipid flux and GDGT-based thermometry in sinking particles of high-latitude oceans: Fram Strait (79°N) and Antarctic Polar Front (50°S). *Biogeosciences* **16**, 2247–2268 (2019).
32. J. A. Smith, C.-D. Hillenbrand, G. Kuhn, R. D. Larter, A. G. C. Graham, W. Ehrmann, S. G. Moreton, M. Forwick, Deglacial history of the West Antarctic Ice Sheet in the western Amundsen Sea Embayment. *Quat. Sci. Rev.* **30**, 488–505 (2011).
33. C.-D. Hillenbrand, S. J. Crowhurst, M. Williams, D. A. Hodell, I. N. McCave, W. Ehrmann, C. Xuan, A. M. Piotrowski, F. J. Hernández-Molina, A. G. C. Graham, H. Grobe, T. J. Williams, J. R. Horrocks, C. S. Allen, R. D. Larter, New insights from multi-proxy data from the West Antarctic continental rise: Implications for dating and interpreting Late Quaternary palaeoenvironmental records. *Quat. Sci. Rev.* **257**, 106842 (2021).
34. W. Majewski, J. Stolarski, P. J. Bart, Two Rare Pustulose/spinose morphotypes of Benthic Foraminifera from Eastern Ross Sea, Antarctica. *J. Foraminifer. Res.* **49**, 405–422 (2019).
35. W. Majewski, P. J. Bart, A. J. McGlannan, Foraminiferal assemblages from ice-proximal paleo-settings in the Whales Deep Basin, eastern Ross Sea, Antarctica. *Palaeogeogr. Palaeoclimatol. Palaeoecol.* **493**, 64–81 (2018).
36. R. Liu, Z. Han, J. Zhao, H. Zhang, D. Li, J. Ren, J. Pan, H. Zhang, Distribution and source of glycerol dialkyl glycerol tetraethers (Gdgts) and the applicability of gdgt-based temperature proxies in surface sediments of prydz bay, east antarctica. *Polar Res.* **39**, 1–15 (2020).
37. N. Lamping, J. Müller, O. Esper, C. D. Hillenbrand, J. A. Smith, G. Kuhn, Highly branched isoprenoids reveal onset of deglaciation followed by dynamic sea-ice conditions in the western Amundsen Sea, Antarctica. *Quat. Sci. Rev.* **228**, 106103 (2020).
38. S. Fietz, L. Ho, C. Huguet, Archaeal membrane lipid-based paleothermometry for applications in Polar Oceans. *Oceanography* **33**, 104–114 (2020).
39. W. Xiao, Y. Xu, C. Zhang, J. Lin, W. Wu, L. Xiaoxia, J. Tan, X. Zhang, F. Zheng, X. Song, Y. Zhu, Y. Yang, H. Zhang, F. Wenzhöfer, A. A. Rowden, R. N. Glud, Disentangling effects of sea surface temperature and water depth on hydroxylated isoprenoid GDGTs: Insights from the hadal zone and global sediments. *Geophys. Res. Lett.* **50**, e2023GL103109 (2023).
40. X. Lü, X.-L. Liu, F. J. Elling, H. Yang, S. Xie, J. Song, X. Li, H. Yuan, N. Li, K.-U. Hinrichs, Hydroxylated isoprenoid GDGTs in Chinese coastal seas and their potential as a paleotemperature proxy for mid-to-low latitude marginal seas. *Org. Geochem.* **89-90**, 31–43 (2015).
41. A. Russo, A. Bergamasco, S. Carniel, L. Grieco, M. Sclavo, G. Spezie, Climatology and decadal variability of the Ross Sea shelf waters. *Adv. Oceanogr. Limnol.* **2**, 55–77 (2011).
42. Y. Wang, M. Zhou, Z. Zhang, M. S. Dinniman, Seasonal variations in Circumpolar Deep Water intrusions into the Ross Sea continental shelf. *Front. Mar. Sci.* **10**, 1020791 (2023).
43. S. T. Belt, L. Smik, T. A. Brown, J.-H. Kim, S. J. Rowland, C. S. Allen, J.-K. Gal, K.-H. Shin, J. I. Lee, K. W. R. Taylor, Source identification and distribution reveals the potential of the geochemical Antarctic sea ice proxy IPSO25. *Nat. Commun.* **7**, 12655 (2016).
44. J. K. Volkman, A review of sterol markers for marine and terrigenous organic matter. *Org. Geochem.* **9**, 83–99 (1986).
45. S. T. Belt, Source-specific biomarkers as proxies for Arctic and Antarctic sea ice. *Org. Geochem.* **125**, 277–298 (2018).
46. P. Spector, J. Stone, S. G. Cowdery, B. Hall, H. Conway, G. Bromley, Rapid early-Holocene deglaciation in the Ross Sea, Antarctica. *Geophys. Res. Lett* **44**, 7817–7825 (2017).
47. A. Cau, C. Ennas, D. Moccia, O. Mangoni, F. Bolinesi, M. Saggiomo, A. Granata, L. Guglielmo, K. M. Swadling, A. Pusceddu, Particulate organic matter release below melting sea ice (Terra Nova Bay, Ross Sea, Antarctica): Possible relationships with zooplankton. *J. Mar. Syst.* **217**, 103510 (2021).
48. M. Saggiomo, L. Escalera, V. Saggiomo, F. Bolinesi, O. Mangoni, Phytoplankton blooms below the Antarctic Landfast Ice During the melt season between late spring and early summer. *J. Phycol.* **57**, 541–550 (2021).
49. A. F. Thompson, A. L. Stewart, P. Spence, K. J. Heywood, The Antarctic slope current in a changing climate. *Rev. Geophys.* **56**, 741–770 (2018).
50. A. L. Stewart, A. F. Thompson, Eddy generation and jet formation via dense water outflows across the Antarctic continental slope. *J. Phys. Oceanogr.* **46**, 3729–3750 (2016).
51. T. W. K. Armitage, R. Kwok, A. F. Thompson, G. Cunningham, Dynamic topography and sea level anomalies of the Southern Ocean: Variability and teleconnections. *J. Geophys. Res. Oceans* **123**, 613–630 (2018).
52. R. Moorman, A. K. Morrison, A. M. Hogg, Thermal responses to Antarctic Ice Shelf Melt in an Eddy-Rich Global Ocean–Sea Ice model. *J. Climate* **33**, 6599–6620 (2020).
53. Y. Nakayama, C. A. Greene, F. S. Paolo, V. Mensah, H. Zhang, H. Kashiwase, D. Simizu, J. S. Greenbaum, D. D. Blankenship, A. Abe-Ouchi, S. Aoki, Antarctic Slope current modulates ocean heat intrusions towards Totten Glacier. *Geophys. Res. Lett.* **48**, e2021GL094149 (2021).
54. S. Schmidtko, K. J. Heywood, A. F. Thompson, S. Aoki, Multidecadal warming of Antarctic waters. *Science* **346**, 1227–1231 (2014).
55. P. Spence, S. M. Griffies, M. H. England, A. M. Hogg, O. A. Saenko, N. C. Jourdain, Rapid subsurface warming and circulation changes of Antarctic coastal waters by poleward shifting winds. *Geophys. Res. Lett.* **41**, 4601–4610 (2014).
56. Y. Wang, E. P. Chassignet, K. Speer, On the dynamics of the Ross Gyre: the relative importance of wind, buoyancy, eddies, and the Antarctic Circumpolar Current. *Front. Mar. Sci.* **11**, 1465808 (2024).
57. R. Tolotti, C. Salvi, G. Salvi, M. C. Bonci, Late Quaternary climate variability as recorded by micropalaeontological diatom data and geochemical data in the western Ross Sea, Antarctica. *Antarct. Sci.* **25**, 804–820 (2013).
58. Y. Si, A. L. Stewart, I. Eisenman, Heat transport across the Antarctic Slope Front controlled by cross-slope salinity gradients. *Sci. Adv.* **9**, eadd7049 (2023).
59. A. Silvano, S. R. Rintoul, B. Peña-Molino, W. R. Hobbs, E. van Wijk, S. Aoki, T. Tamura, G. D. Williams, Freshening by glacial meltwater enhances melting of ice shelves and reduces formation of Antarctic Bottom Water. *Sci. Adv.* **4**, eaap9467 (2018).
60. N. R. Golledge, L. Menviel, L. Carter, C. J. Fogwill, M. H. England, G. Cortese, R. H. Levy, Antarctic contribution to meltwater pulse 1A from reduced Southern Ocean overturning. *Nat. Commun.* **5**, 5107 (2014).
61. D. Swingedouw, T. Fichefet, P. Huybrechts, H. Goosse, E. Driesschaert, M.-F. Loutre, Antarctic ice-sheet melting provides negative feedbacks on future climate warming. *Geophys. Res. Lett.* **35**, L17705 (2008).
62. R. Bintanja, G. J. van Oldenborgh, S. S. Drijfhout, B. Wouters, C. A. Katsman, Important role for ocean warming and increased ice-shelf melt in Antarctic sea-ice expansion. *Nat. Geosci.* **6**, 376–379 (2013).
63. C. Xie, Z. Zhang, Y. Chen, C. Wang, M. Zhou, The response of Ross Sea Shelf water properties to enhanced Amundsen sea ice shelf melting. *J. Geophys. Res. Oceans* **129**, e2024JC020919 (2024).
64. J. Garland, T. R. Jones, M. Neuder, J. W. C. White, E. Bradley, An information-theoretic approach to extracting climate signals from deep polar ice cores. *Chaos* **29**, 101105 (2019).
65. D. P. Lowry, N. R. Golledge, L. Menviel, N. A. N. Bertler, Deglacial evolution of regional Antarctic climate and Southern Ocean conditions in transient climate simulations. *Clim. Past* **15**, 189–215 (2019).
66. S. L. Greenwood, L. M. Simkins, A. R. W. Halberstadt, L. O. Prothro, J. B. Anderson, Holocene reconfiguration and readvance of the East Antarctic Ice Sheet. *Nat. Commun.* **9**, 3176 (2018).
67. L. Herraiz-Borreguero, A. C. N. Garabato, Poleward shift of Circumpolar Deep Water threatens the East Antarctic Ice Sheet. *Nat. Clim. Chang.* **12**, 728–734 (2022).
68. J. Neme, M. H. England, A. McC. Hogg, Projected Changes of Surface Winds Over the Antarctic Continental Margin. *Geophys. Res. Lett.* **49**, e2022GL098820 (2022).
69. P. Dutrieux, J. De Rydt, A. Jenkins, P. R. Holland, H. K. Ha, S. H. Lee, E. J. Steig, Q. Ding, E. P. Abrahamsen, M. Schröder, Strong sensitivity of Pine Island ice-shelf melting to climatic variability. *Science* **343**, 174–178 (2014).
70. J. Lanham, M. Mazloff, A. C. Naveira Garabato, M. Siegert, A. Mashayek, Seasonal regimes of warm Circumpolar Deep Water intrusion toward Antarctic ice shelves. *Commun. Earth Environ.* **6**, 168 (2025).
71. A. Mangini, M. Jung, S. Laukenmann, What do we learn from peaks of uranium and of manganese in deep sea sediments? *Mar. Geol.* **177**, 63–78 (2001).
72. L. Gasperini, G. Stanghellini, SeisPrho: An interactive computer program for processing and interpretation of high-resolution seismic reflection profiles. *Comput. Geosci.* **35**, 1497–1507 (2009).
73. A. R. Loeblich, H. Tappan, *Foraminiferal Genera and Their Classification* (Springer, 1988; http://link.springer.com/10.1007/978-1-4899-5760-3).
74. W. Majewski, J. B. Anderson, Holocene foraminiferal assemblages from Firth of Tay, Antarctic Peninsula: Paleoclimate implications. *Mar. Micropaleontol.* **73**, 135–147 (2009).
75. M. Stuiver, H. A. Polach, Discussion reporting of 14C data. *Radiocarbon* **19**, 355–363 (1977).
76. T. Tesi, S. T. Belt, K. Gariboldi, F. Muschitiello, L. Smik, F. Finocchiaro, F. Giglio, E. Colizza, G. Gazzurra, P. Giordano, C. Morigi, L. Capotondi, A. Nogarotto, D. Köseoğlu, A. Di Roberto, A. Gallerani, L. Langone, Resolving sea ice dynamics in the north-western Ross Sea during the last 2.6 ka: From seasonal to millennial timescales. *Quat. Sci. Rev.* **237**, 106299 (2020).
77. S. T. Belt, T. A. Brown, A. N. Rodriguez, P. C. Sanz, A. Tonkin, R. Ingle, A reproducible method for the extraction, identification and quantification of the Arctic sea ice proxy IP 25 from marine sediments. *Anal. Methods* **4**, 705–713 (2012).
78. R.-Y. Tung, S. L. Ho, Y. Kubota, M. Yamamoto, J. Hefter, C.-C. Shen, Replicability of paleotemperature records in the northern Okinawa Trough and its implications for paleoceanographic reconstructions. *Prog Earth Planet Sci* **11**, 61 (2024).
79. S. Fietz, C. Huguet, G. Rueda, B. Hambach, A. Rosell-Melé, Hydroxylated isoprenoidal GDGTs in the Nordic Seas. *Mar. Chem.* **152**, 1–10 (2013).
80. D. Varma, E. C. Hopmans, Z. R. van Kemenade, S. Kusch, S. Berg, N. J. Bale, F. Sangiorgi, G.-J. Reichart, J. S. Sinninghe Damsté, S. Schouten, Evaluating isoprenoidal hydroxylated GDGT-based temperature proxies in surface sediments from the global ocean. *Geochim. Cosmochim. Acta* **370**, 113–127 (2024).

81. K. Matsuoka, A. Skoglund, G. Roth, J. de Pomereu, H. Griffiths, R. Headland, B. Herried, K. Katsumata, A. Le Brocq, K. Licht, F. Morgan, P. D. Neff, C. Ritz, M. Scheinert, T. Tamura, A. Van de Putte, M. van den Broeke, A. von Deschwanden, C. Deschamps-Berger, B. Van Liefferinge, S. Tronstad, Y. Melvær, Quantarctica, an integrated mapping environment for Antarctica, the Southern Ocean, and sub-Antarctic islands. *Environ. Model. Software* **140**, 105015 (2021).
82. J. Schmitt, R. Schneider, J. Elsig, D. Leuenberger, A. Lourantou, J. Chappellaz, P. Köhler, F. Joos, T. F. Stocker, M. Leuenberger, H. Fischer, Carbon isotope constraints on the deglacial CO_2 rise from ice cores. *Science* **336**, 711–714 (2012).
83. K. Lambeck, H. Rouby, A. Purcell, Y. Sun, M. Sambridge, Sea level and global ice volumes from the Last Glacial Maximum to the Holocene. *Proc. Natl. Acad. Sci. U.S.A.* **111**, 15296–15303 (2014).
84. P. U. Clark, J. D. Shakun, P. A. Baker, P. J. Bartlein, S. Brewer, E. Brook, A. E. Carlson, H. Cheng, D. S. Kaufman, Z. Liu, T. M. Marchitto, A. C. Mix, C. Morrill, B. L. Otto-Bliesner, K. Pahnke, J. M. Russell, C. Whitlock, J. F. Adkins, J. L. Blois, J. Clark, S. M. Colman, W. B. Curry, B. P. Flower, F. He, T. C. Johnson, J. Lynch-Stieglitz, V. Markgraf, J. McManus, J. X. Mitrovica, P. I. Moreno, J. W. Williams, Global climate evolution during the last deglaciation. *Proc. Natl. Acad. Sci. U.S.A.* **109**, E1134–E1142 (2012).

Acknowledgments: We thank S. Moretti, P. Montagna, P. Giordano, L. Langone, and S. Miserocchi for productive discussions; the sorting center of the Italian National Antarctic Museum for providing the sedimentary material; R. Melis for cooperation during the sampling party; F. Adolphi and P. Bohleber for productive discussions regarding the age model construction; the technicians at Alfred Wegener Institute (AWI), Helmholtz Centre for Polar and Marine Research, Bremerhaven, Germany, which assisted during the analysis of the studied samples; and A.Gallerani and the institute of marine sciences (CNR-ISMAR) in Bologna, Italy, which hosted the subsampling of the studied core. **Funding:** T.T. and A.D.R. acknowledge funding by the Programma Nazionale di Ricerche in Antartide (PNRA), grant nos. PNRA19_00018 and PNRA16_00055, respectively. G.M. acknowledges funding from the PAIGE programme (Chronologies for Polar Paleoclimate Archives Italian-German Partnership) funded by Helmholtz. T.T. acknowledges collaboration within the PAIGE framework. **Author contributions:** Conceptualization: T.T., C.P., and S.T.B. Investigation: C.P., T.T., L.C., F.G., A.D.R., and J.H. Data curation: C.P. and T.T., Formal analysis: C.P., T.T., F.B., and F.M. Funding acquisition: T.T. Methodology: C.P., T.T., F.M., A.N., J.H., M.S., L.C., and A.G. Project administration: T.T. and A.D.R. Resources: C.P., T.T., G.M., L.C., F.G., A.D.R., and J.H. Validation: C.P., T.T., and F.G. Visualization: C.P., G.G., and L.C. Software: C.P. Supervision: T.T., G.M., C.P., F.G., and F.M. Writing—original draft: C.P. and T.T. Writing—review and editing: C.P., T.T., A.N., M.S., F.B., F.G., L.C., G.M., J.H., A.D.R., S.T.B., E.P., F.M., A.G., E.C., G.G., and F.T. **Competing interests:** The authors declare that they have no competing interests. **Data and materials availability:** All data needed to evaluate the conclusions in the paper are present in the paper and/or the Supplementary Materials. Additional datasets generated and analyzed in this study have been deposited in Dryad and are available at https://doi.org/10.5061/dryad.rfj6q57mn.

Submitted 8 October 2024
Accepted 23 May 2025
Published 27 June 2025
10.1126/sciadv.adt7075